

Wind load and wind-induced effect of the large wind turbine tower-blade system considering blade yaw and interference

S.T. Ke^{*1,2}, X.H. Wang^{1a} and Y.J. Ge^{2b}

¹Department of Civil Engineering, Nanjing University of Aeronautics and Astronautics, Nanjing 210016, China

²State Key Laboratory for Disaster Reduction in Civil Engineering, Tongji University, Shanghai 200092, China

(Received November 9, 2017, Revised April 13, 2018, Accepted May 18, 2018)

Abstract. The yaw and interference effects of blades affect aerodynamic performance of large wind turbine system significantly, thus influencing wind-induced response and stability performance of the tower-blade system. In this study, the 5MW wind turbine which was developed by Nanjing University of Aeronautics and Astronautics (NUAA) was chosen as the research object. Large eddy simulation on flow field and aerodynamics of its wind turbine system with different yaw angles (0°, 5°, 10°, 20°, 30° and 45°) under the most unfavorable blade position was carried out. Results were compared with codes and measurement results at home and abroad, which verified validity of large eddy simulation. On this basis, effects of yaw angle on average wind pressure, fluctuating wind pressure, lift coefficient, resistance coefficient, streaming and wake characteristics on different interference zone of tower of wind turbine were analyzed. Next, the blade-cabin-tower-foundation integrated coupling model of the large wind turbine was constructed based on finite element method. Dynamic characteristics, wind-induced response and stability performance of the wind turbine structural system under different yaw angle were analyzed systematically. Research results demonstrate that with the increase of yaw angle, the maximum negative pressure and extreme negative pressure of the significant interference zone of the tower present a V-shaped variation trend, whereas the layer resistance coefficient increases gradually. By contrast, the maximum negative pressure, extreme negative pressure and layer resistance coefficient of the non-interference zone remain basically same. Effects of streaming and wake weaken gradually. When the yaw angle increases to 45°, aerodynamic force of the tower is close with that when there's no blade yaw and interference. As the height of significant interference zone increases, layer resistance coefficient decreases firstly and then increases under different yaw angles. Maximum means and mean square error (MSE) of radial displacement under different yaw angles all occur at circumferential 0° and 180° of the tower. The maximum bending moment at tower bottom is at circumferential 20°. When the yaw angle is 0°, the maximum downwind displacement responses of different blades are higher than 2.7 m. With the increase of yaw angle, MSEs of radial displacement at tower top, downwind displacement of blades, internal force at blade roots all decrease gradually, while the critical wind speed decreases firstly and then increases and finally decreases. The comprehensive analysis shows that the worst aerodynamic performance and wind-induced response of the wind turbine system are achieved when the yaw angle is 0°, whereas the worst stability performance and ultimate bearing capacity are achieved when the yaw angle is 45°.

Keywords: large wind turbine system; large eddy simulation; yaw effect, aerodynamic performance; wind-induced response, stability performance

1. Introduction

Due to continuous changes of wind direction and slow rotation of the yaw system, the blade spindle of wind turbine can't align with the inflow wind direction timely, which causes long-term yaw state of the wind turbine (Majid and Fernando 2016, Jeong *et al.* 2013). During normal operation, blade rotation of wind turbine influences wind speed and flow field in a local region surrounding the tower significantly. Researches (Ke *et al.* 2016, Qiang *et al.* 2012) reported that the worst aerodynamic performance of wind turbine system was occurred upon complete

overlapping of occurred upon complete overlapping of blade and tower. Under different yaw states, blades which are at the most unfavorable position cover the tower to different extents. This changes aerodynamic performance wind turbine tower dramatically and thereby affects wind-induced response and stability performance of large wind turbine system. Thus, accurate prediction of wind load and wind-induced effect of large wind turbine system under yaw state has important engineering significance.

For studies concerning wind resistance of large wind turbine system, Ke *et al.* (2016), Hughes *et al.* (2008), Chattot and Jean-Jacques (2008) carried out theoretical calculation and numerical simulation on wind load of single wind turbine. Studies have shown that the blade parking position affected wind load and surrounding flow field of the wind turbine system significantly, and the tower shadow effect reduced generating efficiency of wind turbines. Kuo *et al.* (2016), Hou *et al.* (2016), Hamilton and Cal (2015) made a numerical simulation on streaming in the wind power plant with array of multiple wind turbines and

*Corresponding author, Professor

E-mail: keshitang@163.com

^a Engineer

E-mail: wangxiaohainuaa@163.com

^b Professor

E-mail: yaojunge@tongji.edu.cn

complicated landforms. They studied influencing laws of array mode and landform on wind load and wake of wind turbines. Results provided references for micro-sitting selection of wind power plants. Wang *et al.* (2014) and Murtagh *et al.* (2005) conducted a systematic study on nonlinearity and aeroelastic effect of large wind turbine tower-blade coupling system. They reported that the system had remarkable influences of geometric nonlinearity and considering aeroelastic effect can reflect wind-induced response of large wind turbines more truly. Gallego-Calderon and Natarajan (2015) and Kong *et al.* (2005) conducted a numerical simulation on aerodynamics of large wind turbines under complicated wind conditions and studied fatigue performances of blade and the whole machine based on finite element method. These researches mainly focused on aerodynamics and wind-induced response of large wind turbines under axial incoming wind flow, which was different from actual running state. There are rare studies that discussed variation laws and mechanism of wind load and wind-induced effect of wind turbine system under yaw state.

In this study, the 5MW wind turbine which was developed by Nanjing University of Aeronautics and Astronautics (NUAA) was chosen as the research object. A large eddy simulation on surrounding flow field of the corresponding wind turbine system with different yaw angles (0°, 5°, 10°, 20°, 30° and 45°) when the blade was in the most unfavorable position was carried out. On this basis, effects of yaw angle on surface average wind pressure, fluctuating wind pressure, lift coefficient, resistance coefficient, streaming and wake characteristics of large wind turbine tower were analyzed. Subsequently, dynamic characteristics of the wind turbine system under different yaw angles were analyzed. Moreover, a contrast study on wind-induced dynamic responses and stability performance of the large wind turbine tower-blade coupling system among different yaw angles was implemented by combining complete transient method. Finally, the influencing laws of blade yaw and interference effect on aerodynamics, wind-induced responses and stability of this large wind turbine system were summarized.

2. Calculation methods and project

2.1 Large eddy simulation theory

The flow of fluids needs to obey the basic laws of nature, such as the law of mass conservation, the law of momentum conservation (Newton's second law of motion), the law of energy conservation (first law of thermodynamics), etc.

The law of mass conservation was

$$\frac{\partial \rho}{\partial t} + \frac{\partial \rho u}{\partial x} + \frac{\partial \rho v}{\partial y} + \frac{\partial \rho \omega}{\partial z} = 0 \quad (1)$$

Introducing vector symbols $diva = \frac{\partial a_x}{\partial x} + \frac{\partial a_y}{\partial y} + \frac{\partial a_z}{\partial z}$,

Formula (1) can be written as

$$\frac{\partial \rho}{\partial t} + div(\rho u) = 0 \quad (2)$$

where ρ is the fluid density, t is the time interval, u , v , ω is the speed along x , y and z directions. Eq. (2) shows the continuity equation of transient three-dimensional compressible fluid flow. If the fluid is incompressible, the mass conservation equation was

$$\frac{\partial u}{\partial x} + \frac{\partial v}{\partial y} + \frac{\partial \omega}{\partial z} = 0 \quad (3)$$

The law of momentum conservation was

$$\frac{\partial u}{\partial t} + div(uu) = \frac{\partial \tau_{xx}}{\partial x} + \frac{\partial \tau_{yx}}{\partial y} + \frac{\partial \tau_{zx}}{\partial z} + F_x \quad (4a)$$

$$\frac{\partial v}{\partial t} + div(vu) = \frac{\partial \tau_{xy}}{\partial x} + \frac{\partial \tau_{yy}}{\partial y} + \frac{\partial \tau_{yz}}{\partial z} + F_y \quad (4b)$$

$$\frac{\partial \omega}{\partial t} + div(\omega u) = \frac{\partial \tau_{xz}}{\partial x} + \frac{\partial \tau_{yz}}{\partial y} + \frac{\partial \tau_{zz}}{\partial z} + F_z \quad (4c)$$

where τ_{xx} , τ_{xy} and τ_{xz} were the component of the viscous stress τ ; F_x , F_y and F_z were the volumetric force.

For Newtonian fluids, viscous stress τ is proportional to the rate of deformation of the fluid, then

$$\frac{\partial u}{\partial t} + div(uu) = div(\mu \cdot gradu) - \frac{\partial p}{\partial x} + S_x \quad (5a)$$

$$\frac{\partial v}{\partial t} + div(vu) = div(\mu \cdot gradv) - \frac{\partial p}{\partial y} + S_y \quad (5b)$$

$$\frac{\partial \omega}{\partial t} + div(\omega u) = div(\mu \cdot grad\omega) - \frac{\partial p}{\partial z} + S_z \quad (5c)$$

where $S_x = F_x + s_x$, $S_y = F_y + s_y$, $S_z = F_z + s_z$, the equation of s_x , s_y , and s_z were

$$s_x = \frac{\partial}{\partial x}(\mu \frac{\partial u}{\partial x}) + \frac{\partial}{\partial y}(\mu \frac{\partial u}{\partial y}) + \frac{\partial}{\partial z}(\mu \frac{\partial u}{\partial z}) + \frac{\partial}{\partial x}(\lambda divu) \quad (6a)$$

$$s_y = \frac{\partial}{\partial x}(\mu \frac{\partial u}{\partial y}) + \frac{\partial}{\partial y}(\mu \frac{\partial u}{\partial y}) + \frac{\partial}{\partial z}(\mu \frac{\partial u}{\partial y}) + \frac{\partial}{\partial y}(\lambda divu) \quad (6b)$$

$$s_z = \frac{\partial}{\partial x}(\mu \frac{\partial u}{\partial z}) + \frac{\partial}{\partial y}(\mu \frac{\partial u}{\partial z}) + \frac{\partial}{\partial z}(\mu \frac{\partial u}{\partial z}) + \frac{\partial}{\partial z}(\lambda divu) \quad (6c)$$

Large eddy simulation was accomplished by filter function, which divides the vortex in the flow field into large-scale vortex and small-scale vortex to solve the large-scale vortex directly, while the small-scale vortex adopts the sub-grid model to simulate. Therefore, LES needs to conduct spatial filtering of N-S equation, and incompressible N-S equation under transient state after filtering is as follow

$$\frac{\partial \bar{u}_i}{\partial x_i} = 0 \quad (7)$$

$$\frac{\partial \bar{u}_i}{\partial t} + \frac{\partial}{\partial x_j} (\bar{u}_i \bar{u}_j) = \frac{\partial}{\partial x_j} \left(\mu \frac{\partial \bar{u}_i}{\partial x_j} \right) - \frac{\partial \bar{p}}{\partial x_i} - \frac{\partial \tau_{ij}}{\partial x_j} \quad (8)$$

where \bar{u}_i is velocities along x , y and z directions ($i=1, 2, 3$ are corresponding to x , y and z directions), σ_{ij} is stress tensor caused by molecular viscosity, and τ_{ij} is sub-grid stress. Definitions of σ_{ij} and τ_{ij} were

$$\sigma_{ij} = \left[\mu \left(\frac{\partial \bar{u}_i}{\partial x_j} + \frac{\partial \bar{u}_j}{\partial x_i} \right) \right] - \frac{2}{3} \mu \frac{\partial \bar{u}_i}{\partial x_i} \delta_{ij} \quad (9)$$

$$\tau_{ij} = \overline{u_i u_j} - \bar{u}_i \bar{u}_j \quad (10)$$

Sub-grid stress refers to the momentum transport between filtered small-scale pulsation and solvable large-scale pulsation. It is necessary to construct a sub-grid stress model in order to realize large eddy simulation. According to the basic sub-grid stress model of Smagorinsky (Smagorinsky 1963), the sub-grid stress formula was

$$\tau_{ij} - \frac{1}{3} \tau_{kk} \delta_{ij} = -2 \mu_t \bar{S}_{ij} \quad (11)$$

where μ_t is turbulent viscosity of sub-grid scale, \bar{S}_{ij} is tensor of solvable-scale strain rate, and τ_{kk} is isotropic part of sub-grid stress. The calculation formulas of μ_t and \bar{S}_{ij} were

$$\sigma_{ij} = \left[\mu \left(\frac{\partial \bar{u}_i}{\partial x_j} + \frac{\partial \bar{u}_j}{\partial x_i} \right) \right] - \frac{2}{3} \mu \frac{\partial \bar{u}_i}{\partial x_i} \delta_{ij} \quad (12)$$

$$\tau_{ij} = \overline{u_i u_j} - \bar{u}_i \bar{u}_j \quad (13)$$

where C_s is the Smagorinsky constant which often values in the range of 0.1~0.23. The rate of strain tensor is $|\bar{S}| = \sqrt{2 \bar{S}_{ij} \bar{S}_{ij}}$. Δ is size of spatial grid, $\Delta = (\Delta_x \Delta_y \Delta_z)^{1/3}$. Δ_x , Δ_y and Δ_z are grid sizes along x , y and z directions.

Since the flow field where wind turbine lies is unsteady and turbulent flow is complicated, dynamic Smagorinsky-Lilly model was applied as the sub-grid stress model for large eddy simulation in this study in order simulate surrounding flow field of wind turbine better (Mo *et al.* 2013). In this model, the Smagorinsky constant could be changed dynamically according to microturbulence information. It could capture turbulence characteristics of near wall better and simulate complicated flow field of the wind turbine more accurately (Ángel Jiménez *et al.* 2010).

2.2 Complete transient method

The transient dynamic equilibrium equation of wind turbine system was solved by using the complete transient method (Ke *et al.* 2015). The core was to solve the transient problem by using the implicit algorithm Newmark and HHT. The Newmark algorithm used finite different method. In one time interval, there's

$$M\ddot{\mathbf{u}} + C\dot{\mathbf{u}} + K\mathbf{u} = \mathbf{F}^a \quad (14)$$

$$\dot{\mathbf{u}}_{n+1} = \dot{\mathbf{u}}_n + [(1-\delta)\dot{\mathbf{u}}_n + \delta\ddot{\mathbf{u}}_{n+1}]\Delta t \quad (15)$$

$$\mathbf{u}_{n+1} = \mathbf{u}_n + \dot{\mathbf{u}}_n \Delta t + [(0.5-\alpha)\ddot{\mathbf{u}}_n + \alpha\ddot{\mathbf{u}}_{n+1}]\Delta t^2 \quad (16)$$

where α and δ are Newmark integral parameters; M , K and C were Structural mass matrix, Structural damping matrix and Structural stiffness matrix; \mathbf{u} , $\dot{\mathbf{u}}$ and $\ddot{\mathbf{u}}$ were Structural displacement matrix, Structural Velocity matrix and Structural Acceleration matrix. Calculating the finite element discrete spatial domain by using Newmark algorithm only can't meet the algorithm requirements (the introduced numerical damping shouldn't decrease solving accuracy under high frequency and couldn't produce excessive numerical damping under low frequency). This could be met by combining with HHT algorithm.

The basic HHT method was

$$M\ddot{\mathbf{u}}_{n+1-\alpha_m} + C\dot{\mathbf{u}}_{n+1-\alpha_f} + K\mathbf{u}_{n+1-\alpha_f} = \mathbf{F}_{n+1-\alpha_f}^a \quad (17)$$

where $\ddot{\mathbf{u}}_{n+1-\alpha_m} = (1-\alpha_m)\ddot{\mathbf{u}}_{n+1} + \alpha_m\ddot{\mathbf{u}}_n$,

$$\dot{\mathbf{u}}_{n+1-\alpha_f} = (1-\alpha_f)\dot{\mathbf{u}}_{n+1} + \alpha_f\dot{\mathbf{u}}_n,$$

$$\mathbf{u}_{n+1-\alpha_f} = (1-\alpha_f)\mathbf{u}_{n+1} + \alpha_f\mathbf{u}_n,$$

$$\mathbf{F}_{n+1-\alpha_f}^a = (1-\alpha_f)\mathbf{F}_{n+1}^a + \alpha_f\mathbf{F}_n^a.$$

Wind pressure coefficient which was gained by large eddy simulation was used as the input parameter of wind load time history. Based on complete transient method and ANSYS software platform, wind-induced response time-domain in the wind turbine tower-blade coupling model was calculated. In the model, modal damping was 2% and the loading time steps were 2,048 steps.

2.3 Definition of parameters

The integral formulas of overall lift (crosswind) and resistance (downwind) coefficients of the tower were

$$C_L = \frac{\sum_{i=1}^n C_{P_i} A_i \sin \theta_i}{A} \quad (18)$$

$$C_D = \frac{\sum_{i=1}^n C_{P_i} A_i \cos \theta_i}{A} \quad (19)$$

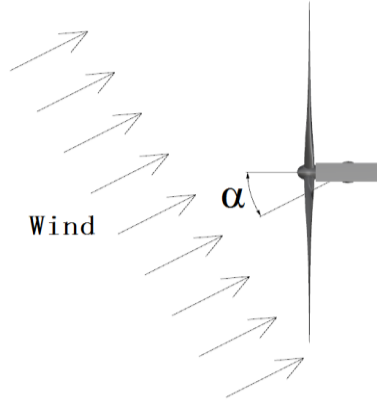


Fig. 1 Yaw angle

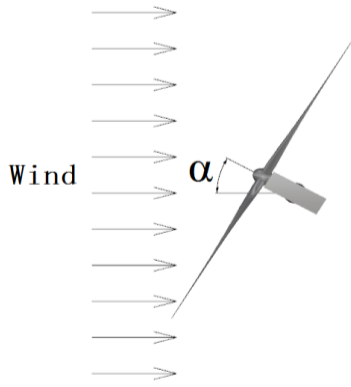


Fig. 2 Equivalent flow field

where A_i is the pressure coverage area of the testing point i , θ_i is the included angle between pressure and wind axis of testing point i , and A is the projection area of the overall structure along the wind axis.

Extreme wind pressure is crucial to local and overall stability checking calculation of large wind turbine towers. It can be expressed as

$$\hat{C}_{pi} = \bar{C}_{pi} \pm g\sigma_{pi} \quad (20)$$

where \hat{C}_{pi} , \bar{C}_{pi} and σ_{pi} are extreme value, mean and mean square error (MSE) of wind pressure coefficient of the testing point i , g is peak factor. In this study, g was 2.5 (GB 50009-2012).

2.4 Brief introduction to the project

Main design parameters and models of the 5MW wind turbine blade and overall machine are shown in Tables 1 and 2. The tower adopted the fixed-length thickness-variable structure. The included angle between any two blades was 120°. Blades distributed uniformly along the circumferential direction. The types of airfoil used are NH02_40, NH02_35, NH02_30, NH02_25, 02_21, NH02_18 and NH02_15. Models of tower, cabin and blades

were constructed successively. Next, the three-dimensional entity model of the large wind turbine was formed by Boolean operation. The included angle between blade spindle of the wind turbine and inflow wind direction was called the yaw angle (Fig. 1). A total of six yaw angles (0°, 5°, 10°, 20°, 30° and 45°) were set, which were denoted as working condition 1, working condition 2, working condition 3, working condition 4, working condition 5 and working condition 6. In large eddy simulation, fixed inflow wind direction and rotating wind turbine model were applied to realize wind field simulations of the large wind turbines under different yaw angles (Fig. 2).

3. CFD numerical simulation

3.1 Computational domain and gridding

To ensure full development of wake of wind turbine, the computational domain was 12D×5D×5D (flow direction X × spanwise Y × vertical direction Z, D is rotor diameter of wind turbine). The wind turbine was put at 3D of entrance of the computational domain. For considerations to computational efficiency and efficiency (Kuo *et al.* 2016, Chattot *et al.* 2009) as well as complexity of blade shape, gridding adopted hybrid grid discretization. The computational domain was divided into local cypher region and periphery region. The local cypher region covered the wind turbine model and was meshed by non-structuralized gridding.

Table 1 Blade parameters of wind turbine

Positio n	Blade span R/m	Chord length C/m	Installation angle $\beta/(^{\circ})$
5	3	2.9	37.14
10	6	3.66	26.672
15	9	4.41	19.069
20	12	4.56	13.692
25	15	4.25	9.83
30	18	3.91	6.976
35	21	3.59	4.802
40	24	3.05	3.103
45	27	2.63	1.742
50	30	2.29	0.63
55	33	1.95	-0.293
60	36	1.75	-1.072
65	39	1.58	-1.736
70	42	1.42	-2.31
75	45	1.27	-2.81
80	48	1.12	-3.25
85	51	0.98	-3.64
90	54	0.83	-3.987
95	57	0.69	-4.299
100	60	0.54	-4.58

Table 2 Main parameters of the 5MW wind turbine generator system


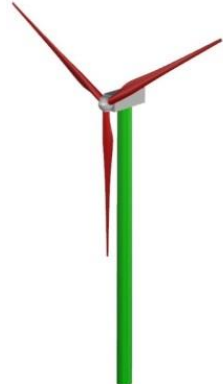
Name of parameters	Numerical value	3D model of blade	3D model of wind turbine
Tower height	124 m		
Top radius	3.0 m		
Bottom radius	3.5 m		
Top thickness	0.06 m		
Bottom thickness	0.15 m		
Blade length	60 m		
Cabin size	18 m×6 m×6 m		
Cut-out wind speed	25.0 m/s		
Yaw rotating speed	0.5°/s		

Table 3 Grid quality and pressure coefficients on windward surface under different gridding schemes

Gridding scheme	1	2	3	4	5
Total number of grids	1.05 millions	5 millions	8 millions	11 millions	30 millions
Grid quality	0.11	0.35	0.51	0.61	0.64
Grid skewness	0.96	0.85	0.80	0.73	0.71
Pressure coefficient on windward surface	1.1	0.96	0.85	0.8	0.79

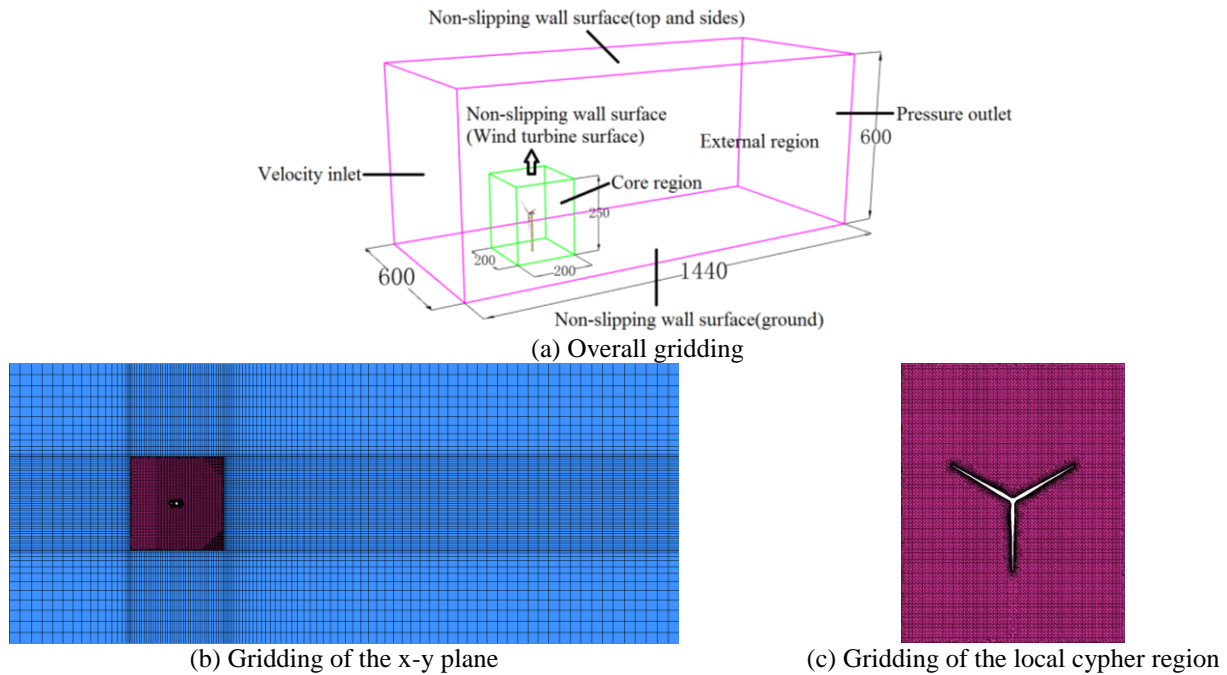


Fig. 3 Computational domain and cipher gridding

The periphery region had regular shapes and was meshed by high-quality structuralized gridding. Grid quality and pressure coefficient on the windward surface under different gridding schemes are shown in Table 3. Grid quality increased gradually as the total number of grids grows, while grid skewness and pressure coefficient on the windward surface declined gradually. The grid quality and

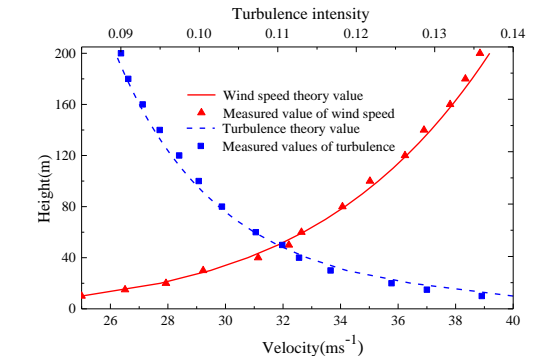
calculated results when the total number of grids was 11 millions and 30 millions were similar. With comprehensive consideration to computational accuracy and efficiency, the total number of grids was determined 11 millions. The computational domain and specific gridding are presented in Fig. 3.

3.2 Boundary conditions and parameters setting

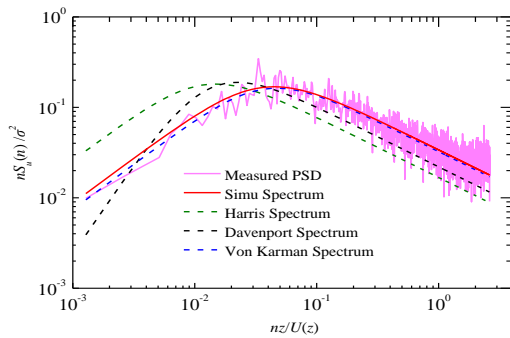
Numerical simulation used 3D single precision and separated solver. Calculating parameters and boundary conditions are shown in Table 4. During service period of wind turbine, influences of gust on overall aerodynamic performance of wind turbine can't be neglected. In order to consider the effect of gust on the aerodynamic performance of the wind turbine system, the index wind profile, turbulence intensity profile and fluctuating wind power spectrums of atmospheric boundary layer were set at velocity inlet according to B type of landform (Fig. 4). The ground roughness index in the wind profile was 0.15 and the basic wind speed at 10 m reference height was 25 m/s. The mean wind profile, turbulence, turbulent kinetic energy, integral turbulence rate and specific dissipation rate were defined by UDF. The large eddy simulation model generates a longitudinally distributed fluctuating wind field at the inlet boundary conditions.

3.3 Validity verification

According to interference degree of downstream tower from upstream blade wake under different yaw angles, the tower was divided into non-interference zone (height=0~64 m) and significant interference zone (height=64~124 m). The lowest surface which blade tip scans was used as the interface.



(a) Profiles of average wind speed and turbulence

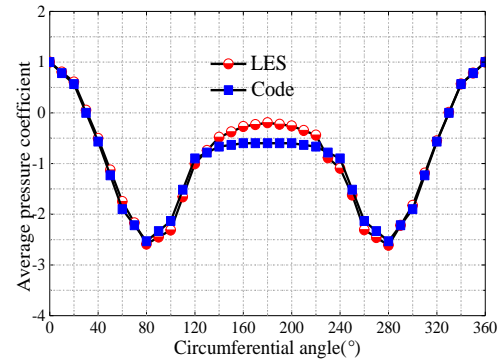


(b) Fluctuating wind power spectrums

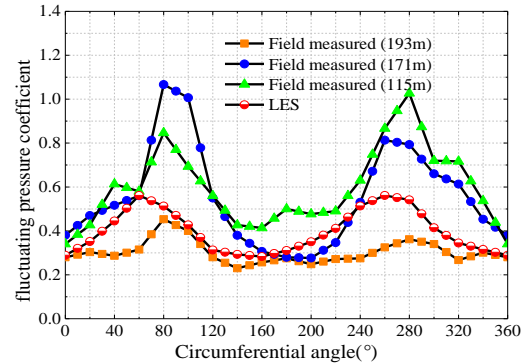
Fig. 4 Comparison of Simulation parameters between LES and the measured results

Table 4 Calculating parameters and boundary conditions

Calculating parameters	Parameter setting
Inlet boundary conditions	Velocity inlet
Outlet boundary conditions	Pressure outlet
Boundary conditions of wall surface	Non-slipping wall surface
Other boundary conditions	Symmetric boundary conditions
Solving method of flow field	SIMPLEC
Sub-grid scale	Dynamic Smagorinsky-Lilly
Discretization of pressure term	Standard format
Transient equation	Second-order implicit expression
Convergence tolerance	10^{-6}
Time step length	0.002s



(a) Average wind pressure



(b) Fluctuating wind pressure

Fig. 5 Comparison of large eddy simulation results, standards and measured results

The position that the tower was facing with inflow wind direction in front under different yaw angles was defined as the 0° of windward surface. Measured data and environmental parameters of large eddy simulation as well as relative errors are shown in Table 5. Distribution curves of circumferential average pressure coefficient and fluctuating pressure coefficient of the typical section in the non-interference zone of the large wind turbine tower are shown in Fig. 5. They were compared with codes and measured curves at home and abroad (Li *et al.* 2015, Nishimura HandTaniike 2001).

Table 5 Measurement data and environmental parameters in large eddy simulation as well as their relative errors

Name of parameters	Field measured in China, 193 m	Field measured in China, 171 m	Field measured in China, 115 m	Large eddy simulation
Inflow wind speed	6.7 m/s	8.4 m/s	10.5 m/s	25 m/s
Wind direction	Easy by south for 20.3°	North by south for 11.5°	East by south for 46.5°	North
Landform	B type	B type	A type	B type
Topographic condition	Flat terrain	Hillside	Small hills at the left side	Open terrain
Relative error	21.06%	41.71%	48.97%	/

According to analysis, (1) the large eddy simulation results of wind turbine tower under different yaw angles were basically consistent with average pressure coefficient of the code along the circumferential direction. Only the average pressure coefficient on the leeside region was slightly lower than the value of standards. (2) Since the measurement was limited by natural wind speed, it was difficult to gain wind load characteristics of wind turbine tower under ultra-high wind velocities. Besides, layout of wind turbine set and surrounding interferences influenced measured fluctuating wind pressure of the wind turbine tower significantly. Thus, large eddy simulation results had certain relative error with measured data. Landform conditions and landform type in the large eddy simulation were similar with measurement at 193 m in China, showing the smallest relative error. In field measurement, fluctuating wind pressure distribution of wind turbine tower was closely related with local landform, layout of wind turbines, inflow wind speed and surrounding interferences. The circumferential distribution law of fluctuating wind pressure was close to measurement results. Numerical values were covered in measurement data. Therefore, the wind load which was gained from large eddy simulation was effective.

4. Analysis of aerodynamic performances

4.1 Characteristics of average wind pressure

Surfaces at 37.2m and 111.6m high of the tower were used as typical sections of non-interference zone and significant interference zone of the tower. The contour map of pressure coefficient and circumferential distribution curves of pressure coefficient on typical sections under different working conditions are shown in Figs. 6 and 7. Some conclusions could be drawn:

1) Under different yaw angles, circumferential distribution trend of pressure coefficient in the non-interference zone was basically consistent and bilateral symmetric. Since the blade couldn't cover the lower tower, positive pressure distribution bands were observed in the range of $\pm 30^\circ$ on the windward surface. The maximum pressure coefficient was observed at 0° of the windward surface. Negative pressure distributions occurred at two sides of the tower and leeside surface. Moreover, the negative pressure at two sides was significantly higher than that on the leeside surface.

2) Due to coverage by blades, negative pressures occurred at 0° of windward surface in the significant interference zone. This negative pressure decreased gradually as yaw angle increased and positive pressure occurred at 30° . The distribution area of positive pressure was interfered by blade and suffered obvious displacement. With the increase of yaw angle, the positive pressure distribution band skewed toward the other side and covered the whole windward surface at 45° .

3) When the yaw angle was relatively small ($0\sim 20^\circ$), negative pressure distributions at two sides of the significant interference zone was different dramatically and had evident asymmetry. With the increase of yaw angle, the maximum negative pressure decreased firstly and then increased.

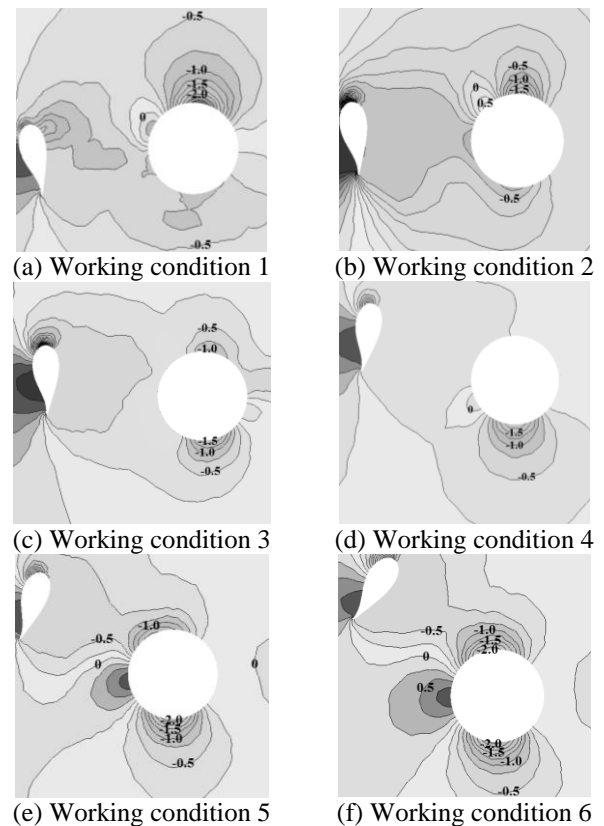


Fig. 6 Contour map of average wind pressure on typical sections of the significant interference zone under different working conditions

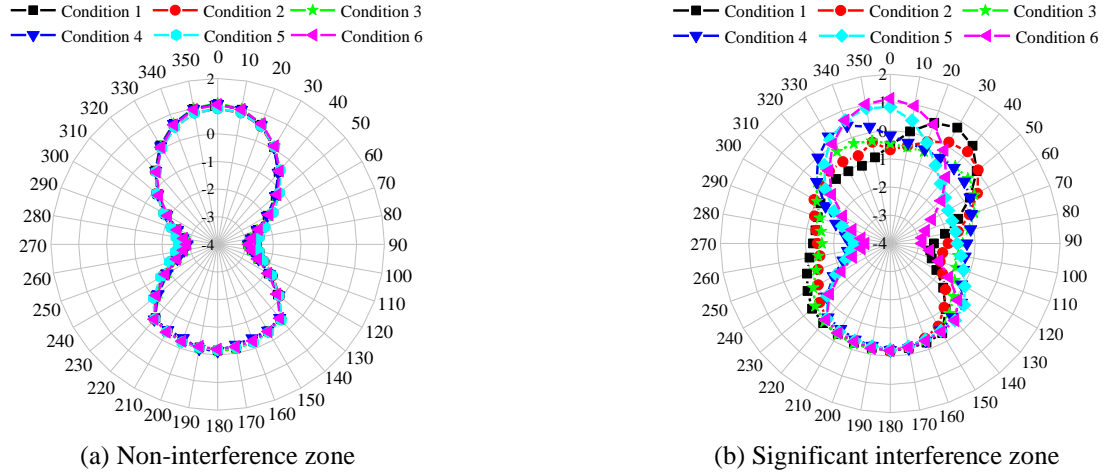


Fig. 7 Circumferential pressure coefficient distribution curves on typical sections under different working conditions

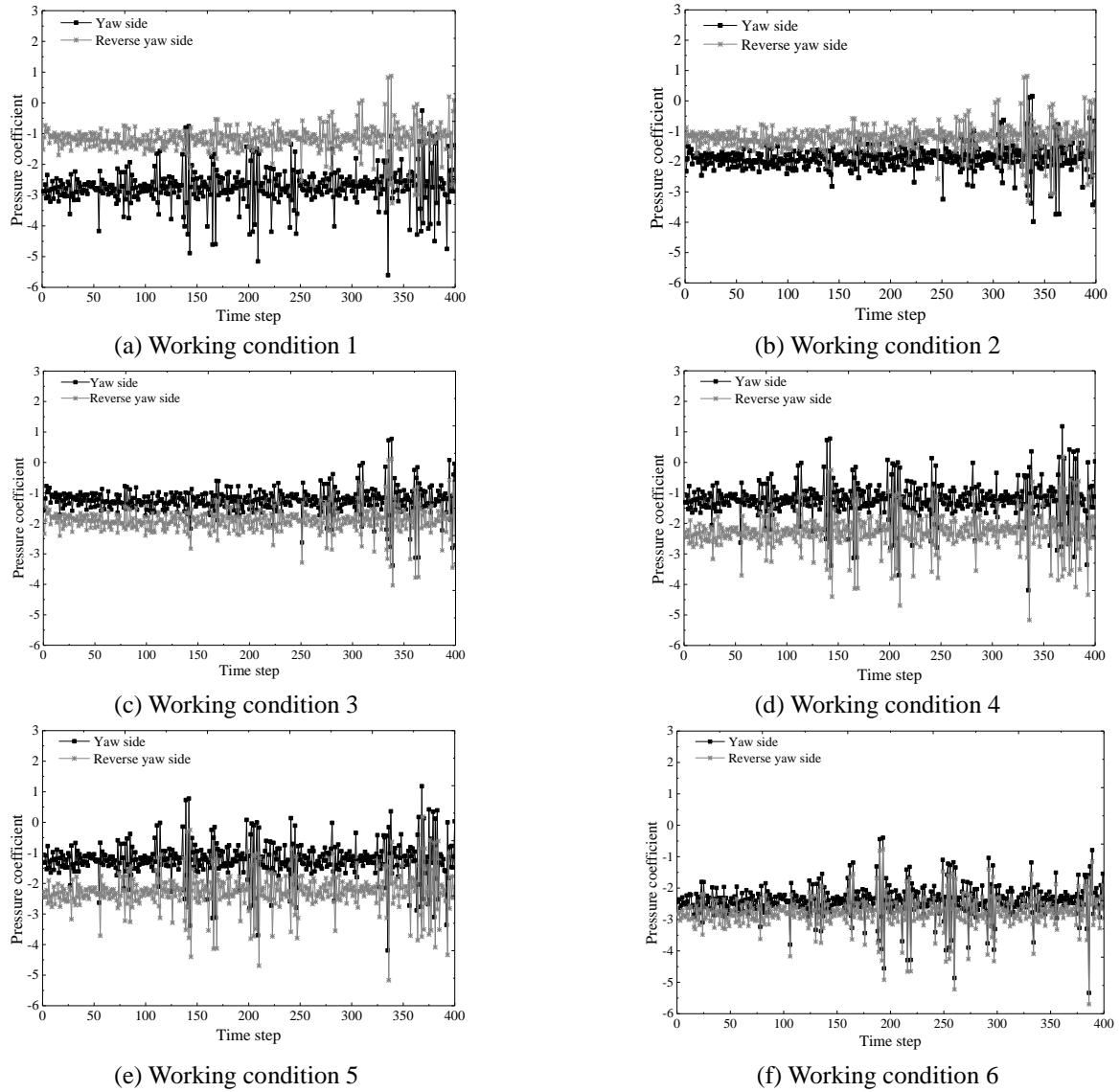


Fig. 8 Time-history curves of pressure coefficients at two sides of the tower under different working conditions

Table 6 Extreme values of wind pressure coefficients at typical measuring points

Height	positions	Working conditions					
		1	2	3	4	5	6
37.2 m	Windward surface	1.80	1.70	1.99	2.00	1.83	2.01
	Crosswind surface	-4.29	-4.03	-4.28	-4.18	-4.10	-4.16
111.6 m	Windward surface	-2.02	-2.17	-1.43	-1.83	1.98	2.34
	Crosswind surface	-3.60	-3.09	-2.80	-3.66	-3.88	-4.36

The maximum negative pressures at two sides of the tower were basically equal and the pressure distribution bands at two sides tended to be symmetric at 45° .

4.2 Characteristics of fluctuating wind pressure

Time-history curves of pressure coefficients at two sides of the tower under different working conditions are shown in Fig. 8. Extreme values of wind pressure coefficient at typical measuring points are listed in Table 6. It found that the negative pressure difference between two sides of the tower was negatively correlated with yaw angle. It was almost 0 at 45° . Under different yaw angles, extreme values of wind pressure on windward surface and leeside surface of the non-interference zone were generally equal. The extreme values on the windward surface of the significant interference zone increased gradually with the increase of yaw angle. The extreme negative pressure on crosswind surface presented a V-shaped variation trend.

4.3 Lift and resistance coefficients

Lift and resistance coefficient curves at different heights under different working conditions are shown in Fig. 9. The ratio between lift coefficient and resistance coefficient is listed in Table 7. It found that:

1) Lift coefficient of non-interference zone was significantly smaller than resistance coefficient under different yaw angles, indicating that the symmetric distribution of pressure coefficient increased resistance coefficient along the flow direction, but offset the lift coefficient along the crosswind direction.

2) In the significant interference zone, the lift coefficient was higher than resistance coefficient under different yaw angles. The maximum ratio was achieved under 0° when the blade covered the tower completely. At the 111.6m section, lift coefficient was 2.74 times of resistance coefficient.

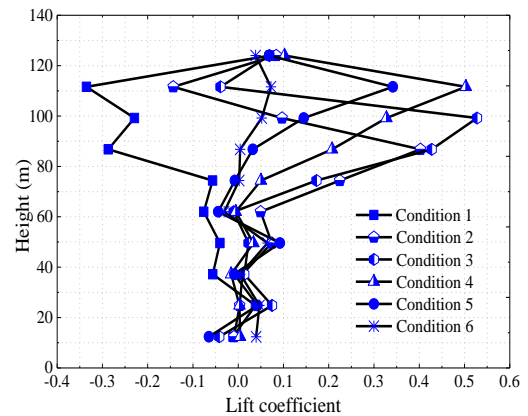
3) Due to small size of blade root, the coverage of blades over the tower top declined. Positive pressure was observed on the windward surface and negative pressure on the leeside surface increased. Resistance coefficient at tower top increased sharply.

4) With the increase of yaw angle, distribution areas of positive pressure on the windward surface and negative pressure at two sides changed significantly. In the significant interference zone, the lift coefficient increased firstly and then decreased, whereas the resistance coefficient grew gradually. With the increase of height of

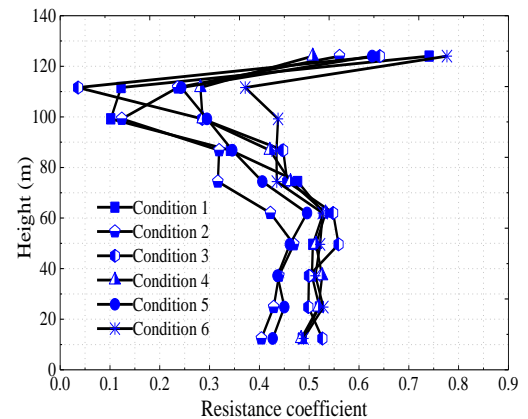
the significant interference zone, resistance coefficient at lower layer decreased firstly and then increased under different yaw angles.

4.4 Characteristics of streaming

Velocity streamlines on typical sections of the non-interference zone and significant interference region are shown in Figs. 10 and 11.



(a) Lift coefficient



(b) Resistance coefficient

Fig. 9 Distribution curves of lift and resistance coefficients under different yaw angles

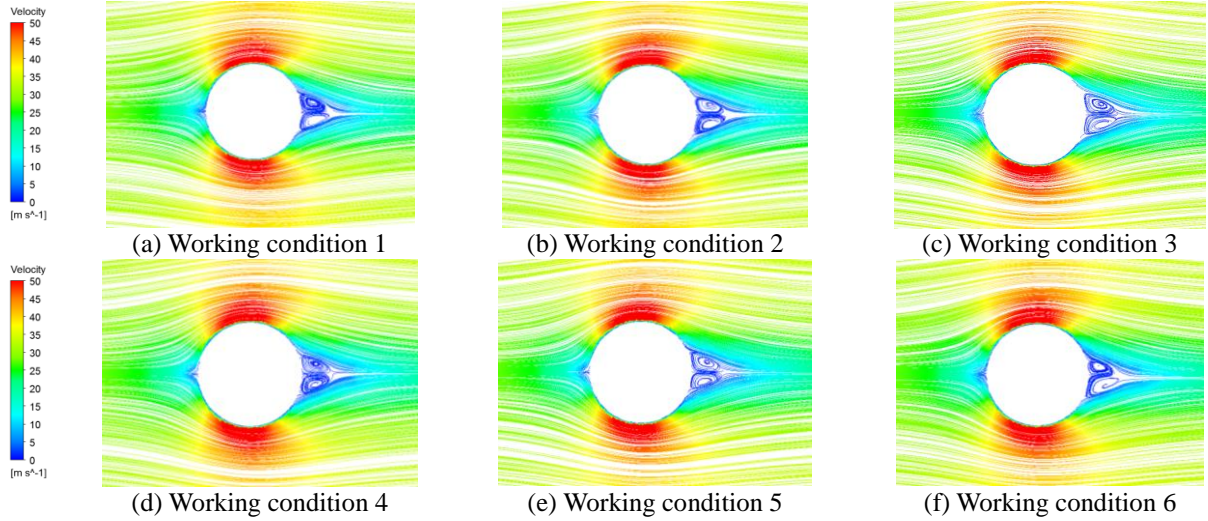


Fig. 10 Velocity streamlines on typical sections in the non-interference zone under different working conditions

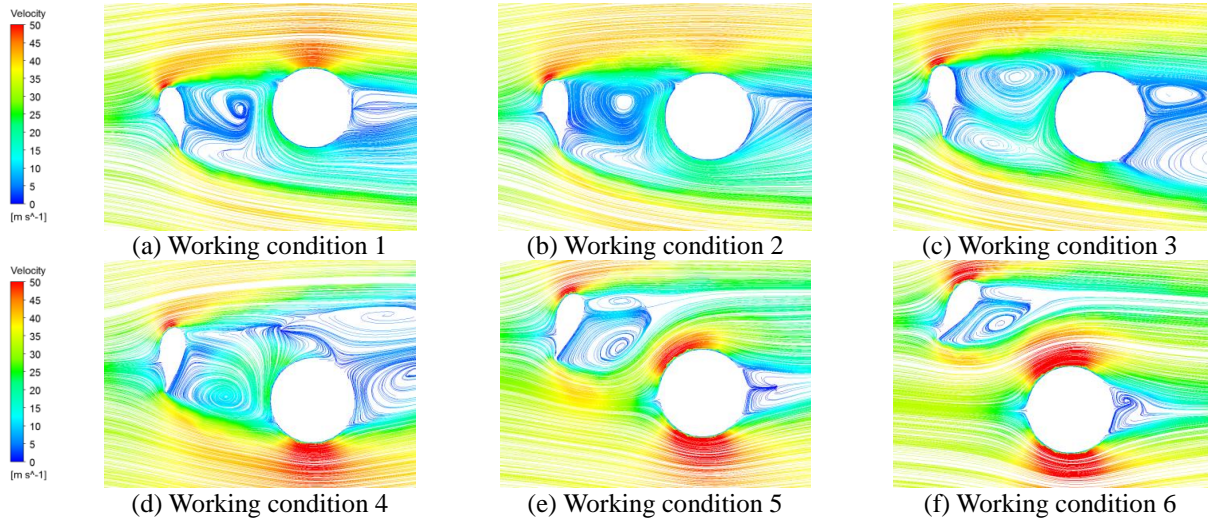


Fig. 11 Velocity streamlines on typical sections in the significant interference zone under different working conditions

Table 7 Ratios between lift coefficient and resistance coefficient at typical sections under different yaw angles

C_L/C_D	Working conditions					
	1	2	3	4	5	6
12.4 m	-0.02	-0.02	-0.08	0.01	-0.15	0.08
24.8 m	0.07	0.01	0.15	0.01	0.10	0.09
37.2 m	-0.11	0.02	0.03	-0.03	-0.02	0.01
49.6 m	-0.08	0.16	0.04	0.07	0.20	0.12
62 m	-0.14	0.12	-0.02	-0.01	-0.09	-0.06
74.4 m	-0.12	0.71	0.38	0.11	-0.02	0.01
86.8 m	-0.84	1.26	0.96	0.49	0.09	0.01
99.2 m	-2.26	0.78	1.85	1.15	0.49	0.12
111.6 m	-2.74	-0.61	-1.09	1.79	1.41	0.19
124 m	0.10	0.15	0.11	0.20	0.11	0.05

By comparison, it found that: 1) in the non-interference zone, inflows all split at 0° of the windward surface under different yaw angles. Such splitting accelerated dramatically at two sides of the tower. Backflow and small-scale eddy were developed on the leeside surface. 2) In the significant interference zone, blade covered the tower to different extents under different yaw angles, which led to great gap of streaming. When the yaw angle was small, blade coverage was remarkable. Inflow split at blades and large-scale eddy was formed between blade and tower. Fluid velocity at two sides of the tower dropped quickly. The splitting point on the windward source skewed, so that the wake skewed and large-scale eddy was developed. 3) With the increase of yaw angle, tower coverage by the blade declined and the inflow split close to 0° of the windward surface, accompanied with formation of a small-scale eddy on the leeside surface. When the yaw angle reached 45° , streaming characteristics of the tower were close to those without blade yaw and interference.

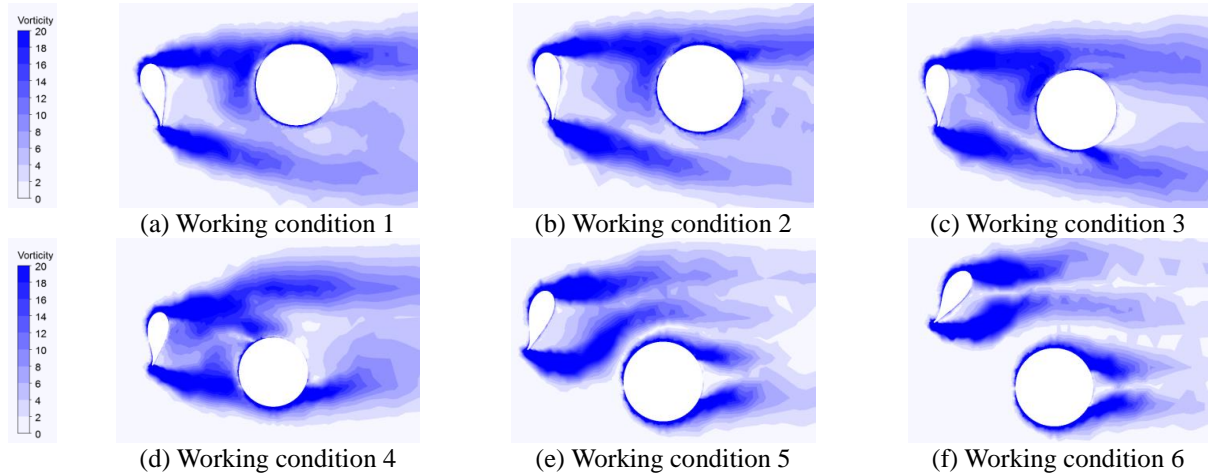


Fig. 12 Vorticity distributions on typical sections under different yaw angles

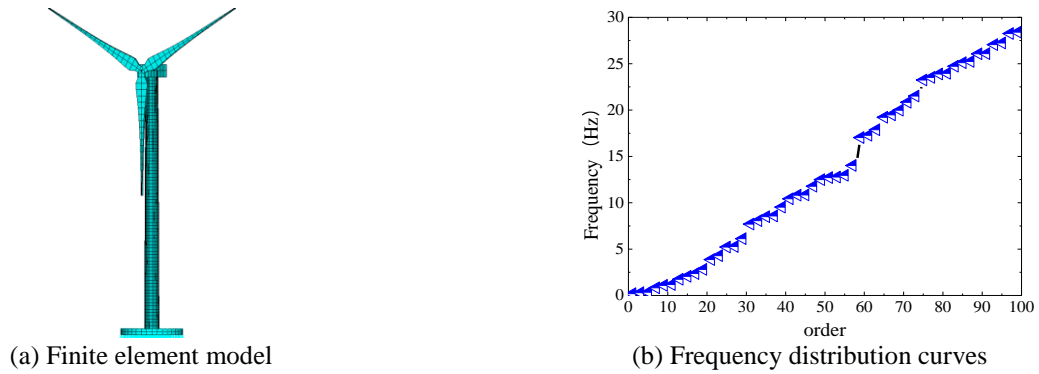


Fig. 13 Wind turbine tower-blade coupling model and frequency distribution curves

Vorticity distributions on typical sections under different working conditions are shown in Fig. 12. Obviously, inflow caused a large area of vorticity growth at blade and tower wake. Mutual interference between blade and tower was different under different yaw angles, which brought significant difference in vorticity distribution. When the yaw angle was small, the tower was in the vorticity growth area at blade wake, so vorticity growth area of the tower changed dramatically and showed significant asymmetry. As yaw angle increased, the vorticity growth area at blade wake went away from the tower gradually. Vorticity growth area of the tower became regular and tended to be symmetric.

5. Analysis of wind-induced response

5.1 Finite element modeling and dynamic performance analysis

A large wind turbine tower-blade integrated finite element model was constructed based on ANSYS platform (Ke *et al.* 2014). Specifically, the tower and blade were simulated by the SHELL63 unit, while the cabin and its internal structure were simulated by beam unit BEAM189 on the whole. The basic unit type of round raft foundation

was SOLID65. The foundation bottom was solidified. Interaction between foundation and base was simulated by the spring unit COMBIN14. Parts were connected through multi-point constraint unit coupling, forming the wind turbine tower-blade integrated finite element model. According to the principle of efficiency-accuracy equilibrium, the model was divided into 4,122 units.

The frequency distribution curves and typical modal shape of wind turbines are shown in Figs. 13 and 14. It can be seen from figures that: 1) the fundamental frequency of the wind turbine tower-blade coupling model was very small (only 0.197Hz). The 10th order of frequency was 1.122Hz and the interval between modals was very small too. 2) The 5th order and 10th order were seesaw motion of three blades. The 30th and 50th orders were complicated seesaw motion and wagging of blades, accompanied with bending deformation of towers. According to analysis of multi-order mode of vibration, the low-order mode of vibration of the wind turbine tower-blade coupling model was dominated by blade deformation. As the vibration frequency increased, seesaw motion and wagging of blade further intensified. Accordingly, there's common deformation of the tower.

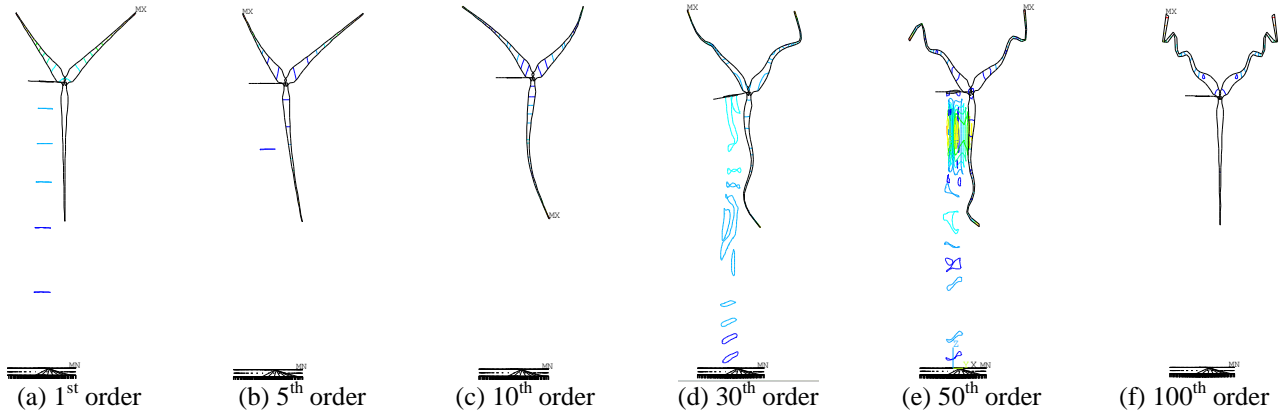


Fig. 14 Typical modal shape of the wind turbine tower-blade coupling model

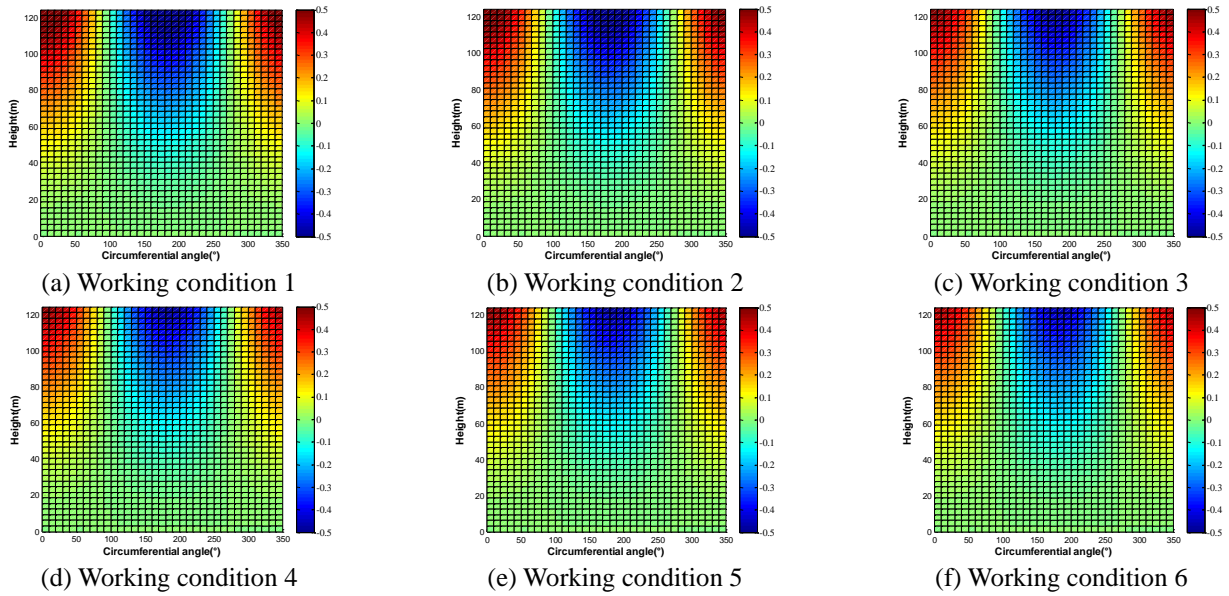


Fig. 15 Average radial displacement of the tower under different working conditions

5.2 Tower response

Radial displacement was displacement of the cylinder shell along the radius direction. It could reflect relative deformation of cylinder shell structures. Negative value represented radial inward and positive value represented radial outward. The average radial displacements of towers under different working conditions are shown in Fig. 15. It found that: 1) average radial displacement of towers showed relatively consistent distribution pattern under different working conditions. Yaw angle mainly influenced middle and upper displacements of the tower. Radial displacement increased gradually as going upward and two extreme value regions were formed in the range of windward surface and leeward surface. The maximum positive and negative displacements were at 0° and 180° of the tower top. 2) With the increase of yaw angle, the maximum average radial displacement at tower top decreased gradually. The average radial displacements under working condition 1 and working condition 6 were 0.589 m and 0.466 m,

respectively. The extreme value region of tower displacement presented a gradual reduction trend. It was above 80 m of the tower under working condition 1 and above 100 m of the tower under working condition 6.

MSEs of radial displacement under different working conditions are exhibited in Fig. 16. The MSE of radial displacement increased gradually as going upward. Two extreme value regions were formed in the range of the windward surface and leeward surface. The maximum MSEs were at 0° and 180° of the tower top. The maximum MSE under working condition 1 and working condition 6 were 0.206 m and 0.096 m, respectively.

Eigenvalues of bending moment at tower bottom under different working conditions are shown in Fig. 17. The distribution laws of average radial and circumferential bending moments at tower bottom basically agree with numerical values under different working conditions. The minimum and maximum bending moments were at 0° and 20° of the tower. MSEs of radial and circumferential bending moments presented consistent distribution laws.

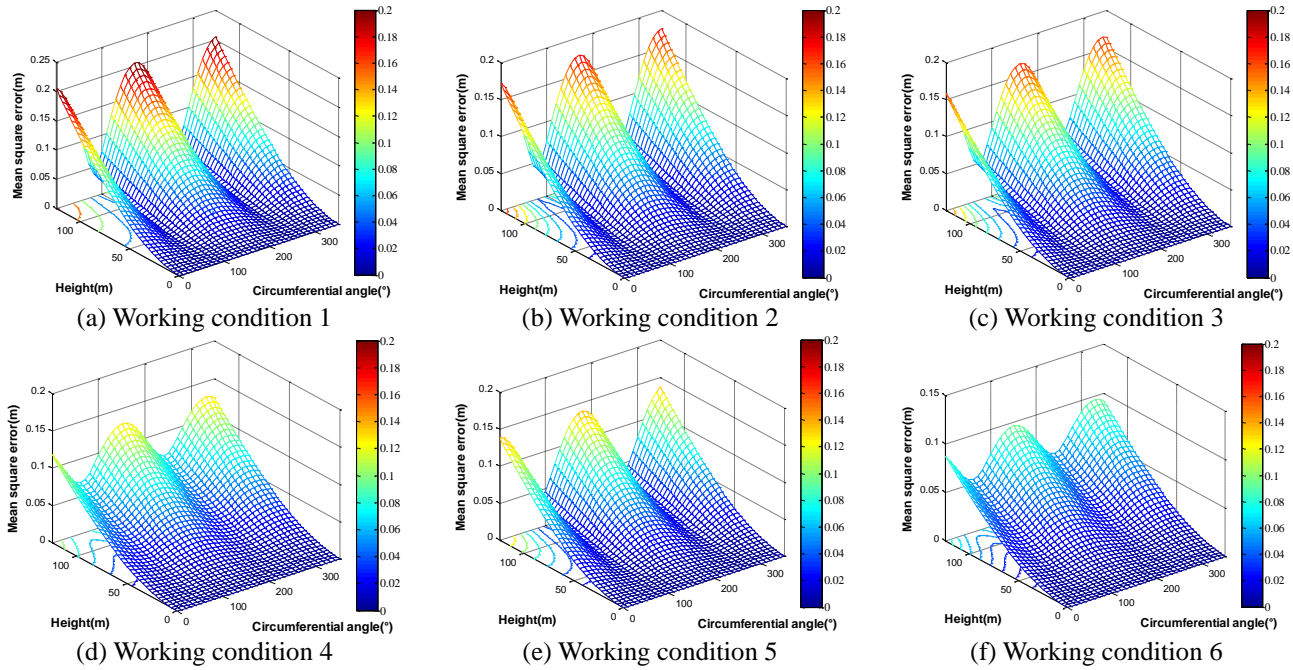


Fig. 16 MSE of radial displacement under different working conditions

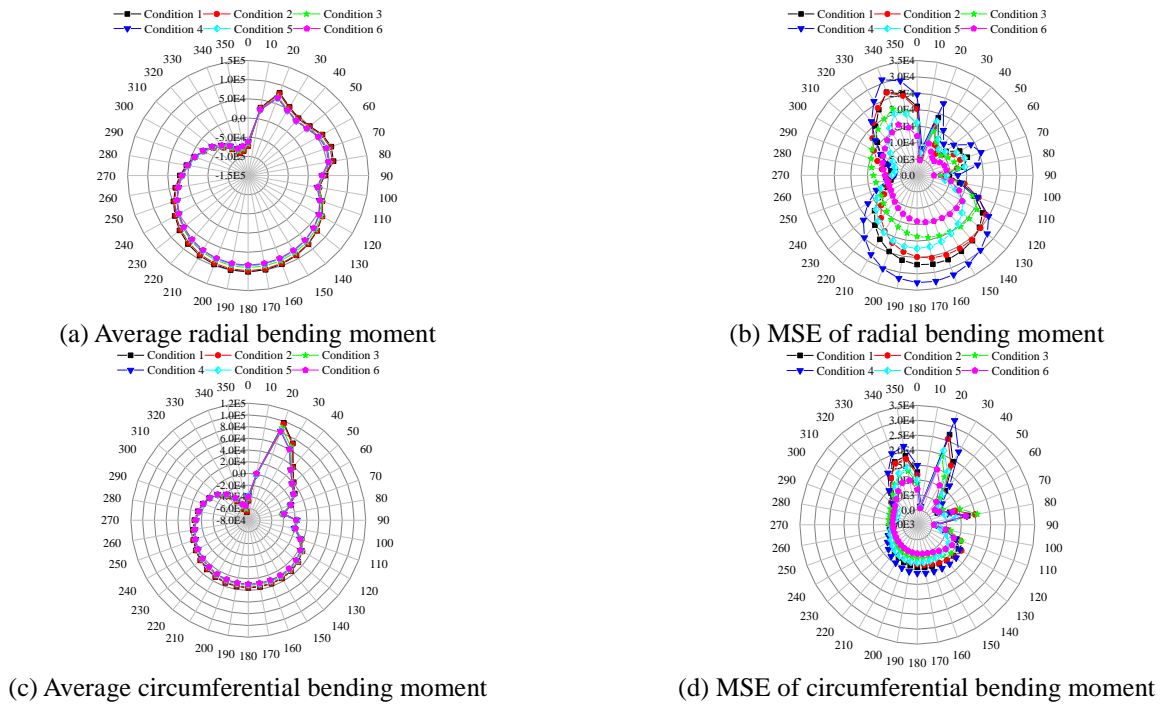


Fig. 17 Eigenvalues of bending moment at tower bottom under different working conditions

However, the numerical values of MSE differed significantly at 0° , 20° , 90° and 340° . The numerical value of MSE under working condition 4 was the largest.

5.3 Blade response

The blade overlapping with the tower was defined the blade 1, while blades of clockwise rotation were blade 2

and 3, respectively. Eigenvalues of windward displacement of different blades under different working conditions are listed in Table 8. The peak factor was 2.5. It can be known from Table 8 that: 1) the windward average displacement and extreme values of blade 1 decreased gradually as yaw angle increased. The extreme value under working condition 1 was the largest (2.79 m) and the extreme value under working condition 6 was the smallest (1.69 m).

Table 8 Eigenvalues of windward displacement of blades under different working conditions

Working conditions	Displacement (m)								
	Blade 1			Blade 2			Blade 3		
	Mean	MSE	Extreme values	Mean	MSE	Extreme values	Mean	MSE	Extreme values
1	-1.36	0.57	-2.79	-1.96	0.62	-3.51	-1.98	0.70	-3.73
2	-1.21	0.44	-2.31	-1.83	0.57	-3.26	-1.86	0.63	-3.44
3	-1.18	0.54	-2.53	-1.88	0.65	-3.51	-1.96	0.74	-3.63
4	-1.20	0.48	-2.40	-1.92	0.58	-3.37	-1.82	0.60	-3.32
5	-0.85	0.43	-1.93	-1.51	0.50	-2.76	-1.62	0.57	-3.05
6	-0.81	0.35	-1.69	-1.4	0.43	-2.48	-1.51	0.49	-2.74

Table 9 Eigenvalues of internal force at root of blade under different working conditions

Working conditions	Shearing force/kN		$M_x/ (kN \cdot m)$		$M_y/ (kN \cdot m)$	
	Mean	MSE	Mean	MSE	Mean	MSE
1	363.16	122.56	11795.51	4948.00	974.11	400.15
2	341.83	117.28	10555.50	3167.14	870.09	260.75
3	281.92	108.65	8427.78	3875.67	697.06	320.12
4	276.40	103.13	8382.00	4571.76	693.23	374.45
5	230.91	98.78	6327.33	3305.34	523.33	271.51
6	212.55	94.15	6076.40	2435.79	501.78	197.18

2) With the increase of yaw angle, average value, MSE and extreme value of windward displacements of blade 2 and blade 3 decreased firstly and then increased and finally decreased. The maximum extreme values of blade 2 and blade 3 under working condition 1 were 3.51 m and 3.73 m, respectively. 3) Extreme values of windward displacements of all three blades under working condition 1 were higher than 2.7 m. Under this circumstance, the mutual interference between tower and blade was the most distinctive.

Eigenvalues of internal force at root of blade 1 under different working conditions are listed in Table 9. It found that the average shearing force and bending moment at root of blades decreased gradually as yaw angles increased. The average value of internal force under working condition 1 was the highest and the average value of internal force under working condition 6 was the smallest. MSE of internal force response under working condition 1 and 4 were relatively high.

6. Wind-induced stability analysis

6.1 Buckling stability

Relationships between buckling maximum displacement and critical wind speed of the wind turbine tower-blade coupling system under different working conditions are shown in Fig. 18. Yaw angle influenced buckling maximum displacement and critical wind speed of the coupling system significantly. With the increase of yaw angle, buckling maximum displacement and critical wind speed decreased

firstly and then increased and finally decreased gradually. The maximum values were occurred under working condition 3 and working condition 1. According to influences of buckling maximum displacement and critical wind speed on buckling stability of the coupling, the working condition was the easiest to suffer buckling failure. The best buckling stability was achieved under working condition 1.

6.2 Ultimate bearing capacity

Variations of wind turbine displacement with wind speed under different working conditions are shown in Fig. 19. It found that: 1) with gradual loading of wind speed, the maximum displacements under working conditions 1, 2 and 3 increased firstly and then dropped sharply and finally increased slightly.

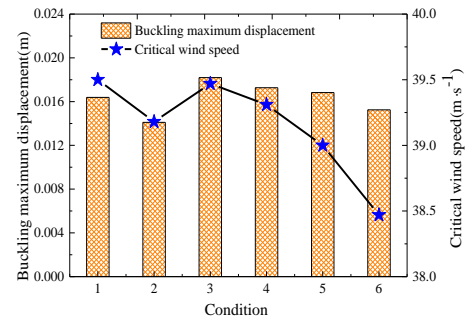


Fig. 18 buckling maximum displacement and critical wind speed of wind turbine under different working conditions

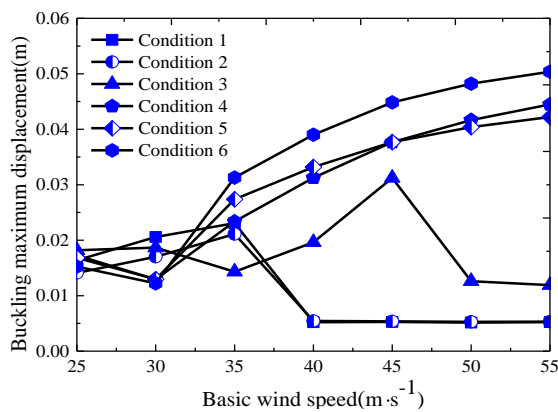


Fig. 19 Variations of wind turbine displacement with wind speed under different working conditions

The maximum displacements under working conditions 4, 5 and 6 decreased firstly and then increased gradually. The maximum displacements under working conditions 4, 5 and 6 were significantly higher than those under working conditions 1, 2 and 3. The maximum displacement under working condition 6 was 0.05 m. 2) As wind speed increased, “reserve effect (sharp reduction of maximum displacement)” were developed under working conditions 1, 2 and 3, but hadn’t under rest three working conditions. Larger yaw angle led to the lower ultimate bearing capacity of the wind turbine system.

7. Conclusions

This study chose a 5MW super-large wind turbine system as the research object. It carried out a numerical simulation on its flow field characteristics and wind effect under six yaw angles (0°, 5°, 10°, 20°, 30° and 45°) when the blade is at the most unfavorable position by combining large eddy simulation and finite element complete transient method. The influencing laws of yaw and blade interference effect on aerodynamic performances, wind-induced response and stability performance of the large wind turbine system were extracted. The following conclusions could be drawn:

1) In the significant interference zone of the tower, the maximum negative pressure and extreme negative pressure present V-shaped variations and the layer resistance coefficient increases gradually. In the non-interference zone, the maximum negative pressure, extreme negative pressure and layer resistance coefficient change slightly. As the significant interference zone climbs up of the tower, layer resistance coefficient decreases firstly and then increases under different yaw angles.

2) When the yaw angle is 0°, the mutual interference between tower and blade in the wind turbine system is the most obvious. Under this circumstance, the ratio between lift coefficient and resistance coefficient is the highest. With the increase of yaw angle, the mutual interference between tower and blade declines gradually. Influences of tower streaming and wake are weakened. When the yaw angle is

45°, aerodynamics of the tower is relatively close to that without blade yaw and interference.

3) When the blade and tower overlap completely (yaw angle=0°), the maximum average radial displacement at tower top and average windward displacement of blade are achieved (0.589 m and 2.79 m, respectively). As yaw angle increases, mean values and MSEs of radial displacement at tower top, windward displacement of blades and internal force at blade root decrease gradually. The buckling maximum displacement and critical wind speed of the wind turbine system decrease firstly and then increase and finally decrease. The ultimate bearing capacity declines gradually.

To sum up, the most remarkable mutual interference between blade and tower is achieved when yaw angle is 0°. The worst aerodynamic performance and wind-induced responses of the wind turbine system are achieved when the yaw angle is 0°. The worst stability performance and ultimate bearing capacity of the wind turbine system are achieved when the yaw angle is 45°. Research conclusions provide references for wind resistance design of large wind turbine system under yaw states.

Acknowledgments

This work was jointly funded by the National Basic Research Program of China (“973” Program) under Grant (2014CB046200), Natural Science Foundation of China (51878351, 51761165022, U1733129), open fund for Jiangsu Key Laboratory of Hi-Tech Research for Wind Turbine Design (ZAA1400206), Jiangsu Outstanding Youth Foundation (BK20160083), and China Postdoctoral Science Foundation (2015T80551).

References

- Chattot, J.J. (2008), “Tower shadow modelization with helicoidal vortex method”, *Comput. Fluids*, **37**(5), 499-504.
- Chattot, J.J. (2009), “Effects of blade tip modifications on wind turbine performance using vortex model”, *Comput. Fluid.*, **38**(7), 1405-1410.
- Gallejo-Calderon, J. and Natarajan, A. (2015), “Assessment of wind turbine drive-train fatigue loads under torsional excitation”, *Eng. Struct.*, **103**(15), 189-202.
- GB 50009-2012 (2012), Load code for the design of building structures, The Ministry of Structure of the People's Republic of China, Beijing.(In Chinese).
- Hamilton, N. and Cal, R.B. (2015), “Anisotropy of the Reynolds stress tensor in the wakes of wind turbine arrays in Cartesian arrangements with counter-rotating rotors”, *Phys. Fluid.*, **27**(1), 013106-24.
- Hou, P., Hu, W., Chen, C., Soltani, M. and Chen, Z. (2016), “Optimization of offshore wind farm layout in restricted zones”, *Energy*, **113**, 487-496.
- Hughes, F.M., Anaya-Lara, O., Ramtharan, G., Jenkins, N. and Strbac, G. (2008), “Influence of tower shadow and wind turbulence on the performance of power system stabilizers for DFIG-based wind farms”, *IEEE T. Energ. Convers.*, **23**(2), 519-528.
- Jeong, M.S., Kim, S.W., Lee, I., Yoo, S.J. and Park, K.C. (2013), “The impact of yaw error on aeroelastic characteristics of a horizontal axis wind turbine blade”, *Renew. Energ.*, **60**(5), 256-

- 268.
- Jiménez, A., Crespo, A. and Migoya, E. (2010), "Application of a LES technique to characterize the wake deflection of a wind turbine in yaw", *Wind Energy*, **13**(6), 559-572.
- Ke, S.T., Wang, T.G., Ge, Y.J. and Tamura, Y. (2014), "Wind-induced responses and equivalent static wind loads of tower-blade coupled large wind turbine system", *Struct. Eng. Mech.*, **52**(3), 485-505.
- Ke, S.T., Wang, T.G., Ge, Y.J., *et al.* (2015), "Aeroelastic Responses of ultra Large Wind Turbine tower-blade coupled structures with SSI Effect", *Adv. Struct. Eng.*, **18**(12), 2075-2087.
- Ke, S.T., Yu, W., Wang, T.G., Ge, Y.J. and Tamura, Y. (2017), "The effect of blade positions on the aerodynamic performances of wind turbine system", *Wind Struct.*, **24**(3):205-221.
- Ke, S.T., Yu, W., Wang, T.G., Zhao, L. and Ge, Y.J. (2016), "Wind loads and load-effects of large scale wind turbine tower with different halt positions of blade", *Wind Struct.*, **23**(6), 559-575.
- Kong, C., Bang, J. and Sugiyama, Y. (2005), "Structural investigation of composite wind turbine blade considering various load cases and fatigue life", *Energy*, **30**(11), 2101-2114.
- Kuo, J.Y.J., Romero, D.A., Beck, J.C. and Amon, C.H. (2016), "Wind farm layout optimization on complex terrains – Integrating a CFD wake model with mixed-integer programming", *Appl. Energ.*, **178**, 404-414.
- Li, X.N., Lu, Y., Liu, Q.K., *et al.* (2015), "Experimental study on wind-included interference effects of circular section chimneys", *Eng. Mech.*, **1**, 159-162. (In Chinese).
- Majid, B. and Fernando, P.A. (2016), "Experimental and theoretical study of wind turbine wakes in yawed conditions", *J. Fluid Mech.*, **806**, 506-541.
- Mo, J.O., Choudhry, A., Arjomandi, M., Kelso, R. and Lee, Y.H. (2013), "Effects of wind speed changes on wake instability of a wind turbine in a virtual wind tunnel using large eddy simulation", *J. Wind Eng. Ind. Aerod.*, **117**(117), 38-56.
- Nishimura, H. and Taniike, Y. (2001), "Aerodynamic characteristics of fluctuating forces on a circular cylinder", *J. Wind Eng. Ind. Aerod.*, **89**(1), 713-723.
- Smagorinsky, J. (1963), "General circulation experiments with the primitive equations", *Mon. Weather Rev.*, **91**(3), 99-164.
- Wang, L., Liu, X., Renevier, N., Stables, M. and Hall, G.M. (2014), "Nonlinear aeroelastic modelling for wind turbine blades based on blade element momentum theory and geometrically exact beam theory", *Energy*, **76**(76), 487-501.
- Wang, Q., Zhou, H. and Wan, D. (2012), "Numerical Simulation of Wind Turbine Blade-Tower Interaction", *J. Mar. Sci. Appl.*, **11**(3), 321-327.

Nomenclature

ρ	Fluid density
t	Time interval
u	Velocity along x directions
v	velocity along y directions
w	velocity along z directions
τ_{xx}	Component of the viscous stress τ
c_p	Specific heat capacity of the fluid
T	Temperature of the fluid
σ_{ij}	Stress tensor
τ_{ij}	SGS
μ_t	Turbulent viscosity of SGS
$\overline{S_{ij}}$	Tensor of solvable-scale strain rate
τ_{kk}	Isotropic part of SGS
C_s	Smagorinsky constant
Δx	Grid sizes along x directions
Δy	Grid sizes along y directions.
\hat{C}_{pi}	Extreme value of pressure coefficient
Δz	Grid sizes along z directions.
\mathbf{M}	Structural mass matrix
\mathbf{C}	Structural damping matrix
\mathbf{K}	Structural stiffness matrix
\mathbf{u}	Structural displacement matrix
$\dot{\mathbf{u}}$	Structural Velocity matrix
$\ddot{\mathbf{u}}$	Structural Acceleration matrix
Δt	Time interval
α, δ	Newmark integral parameters
\mathbf{F}	Load matrix
C_L	Lift coefficient
C_D	Drag coefficient
C_{pi}	pressure coefficient
δ_{pi}	MSE of pressure coefficient
g	Peak factor
A_i	pressure coverage area
\bar{C}_{pi}	Mean of pressure coefficient